NASA/TM—2016-219092

Supercooled Liquid Water Content Instrument Analysis and Winter 2014 Data With Comparisons to the NASA Icing Remote Sensing System and Pilot Reports

Michael C. King
Glenn Research Center, Cleveland, Ohio

April 2016

NASA STI Program . . . in Profile

Since its founding, NASA has been dedicated to the advancement of aeronautics and space science. The NASA Scientific and Technical Information (STI) Program plays a key part in helping NASA maintain this important role.

The NASA STI Program operates under the auspices of the Agency Chief Information Officer. It collects, organizes, provides for archiving, and disseminates NASA's STI. The NASA STI Program provides access to the NASA Technical Report Server—Registered (NTRS Reg) and NASA Technical Report Server—Public (NTRS) thus providing one of the largest collections of aeronautical and space science STI in the world. Results are published in both non-NASA channels and by NASA in the NASA STI Report Series, which includes the following report types:

- TECHNICAL PUBLICATION. Reports of completed research or a major significant phase of research that present the results of NASA programs and include extensive data or theoretical analysis. Includes compilations of significant scientific and technical data and information deemed to be of continuing reference value. NASA counter-part of peer-reviewed formal professional papers, but has less stringent limitations on manuscript length and extent of graphic presentations.

- TECHNICAL MEMORANDUM. Scientific and technical findings that are preliminary or of specialized interest, e.g., "quick-release" reports, working papers, and bibliographies that contain minimal annotation. Does not contain extensive analysis.

- CONTRACTOR REPORT. Scientific and technical findings by NASA-sponsored contractors and grantees.

- CONFERENCE PUBLICATION. Collected papers from scientific and technical conferences, symposia, seminars, or other meetings sponsored or co-sponsored by NASA.

- SPECIAL PUBLICATION. Scientific, technical, or historical information from NASA programs, projects, and missions, often concerned with subjects having substantial public interest.

- TECHNICAL TRANSLATION. English-language translations of foreign scientific and technical material pertinent to NASA's mission.

For more information about the NASA STI program, see the following:

- Access the NASA STI program home page at http://www.sti.nasa.gov

- E-mail your question to help@sti.nasa.gov

- Fax your question to the NASA STI Information Desk at 757-864-6500

- Telephone the NASA STI Information Desk at 757-864-9658

- Write to:
  NASA STI Program
  Mail Stop 148
  NASA Langley Research Center
  Hampton, VA 23681-2199

NASA/TM—2016-219092

Supercooled Liquid Water Content Instrument Analysis and Winter 2014 Data With Comparisons to the NASA Icing Remote Sensing System and Pilot Reports

Michael C. King
Glenn Research Center, Cleveland, Ohio

National Aeronautics and
Space Administration

Glenn Research Center
Cleveland, Ohio 44135

April 2016

Level of Review: This material has been technically reviewed by technical management.

Available from

NASA STI Program
Mail Stop 148
NASA Langley Research Center
Hampton, VA 23681-2199

National Technical Information Service
5285 Port Royal Road
Springfield, VA 22161
703-605-6000

This report is available in electronic form at http://www.sti.nasa.gov/ and http://ntrs.nasa.gov/

Supercooled Liquid Water Content Instrument Analysis and Winter 2014 Data With Comparisons to the NASA Icing Remote Sensing System and Pilot Reports

Michael C. King
National Aeronautics and Space Administration
Glenn Research Center
Cleveland, Ohio 44135

Abstract

The National Aeronautics and Space Administration (NASA) has developed a system for remotely detecting the hazardous conditions leading to aircraft icing in flight, the NASA Icing Remote Sensing System (NIRSS). Newly developed, weather balloon-borne instruments have been used to obtain in-situ measurements of supercooled liquid water during March 2014 to validate the algorithms used in the NIRSS. A mathematical model and a processing method were developed to analyze the data obtained from the weather balloon soundings. The data from soundings obtained in March 2014 were analyzed and compared to the output from the NIRSS and pilot reports.

1.0 Introduction

Inflight icing of aircraft is an issue for the aviation community. Providing operators with near real-time information of hazardous conditions aloft is a possible route to protecting aircraft in flight. The NASA Icing Remote Sensing System (NIRSS), which NASA has been developing, can potentially provide information to pilots and air traffic controllers regarding icing conditions aloft. The focus of the research effort is now shifting to validating the NIRSS system algorithms, driving the work presented in this document.

To support NIRSS validation efforts, weather balloons were released from the NASA Glenn Research Center (GRC) in March 2014 during periods when icing conditions were indicated by forecasts and the NIRSS ground instrumentation. The weather balloons carried specialized, disposable instrument packages, known as radiosondes, to provide in-situ measurements of atmospheric conditions aloft. These radiosondes included an additional, specialized sensor designed to measure supercooled liquid water content (SLWC).

The plan behind the March 2014 weather balloon effort was to concurrently collect upper air data during hazardous in flight icing weather events with both the in-situ and the remote sensing systems. The two objectives were to test procedures and build expertise within NASA with the weather balloon sounding systems, and to develop the necessary analytical methods and tools to analyze the data from the SLWC sensors in preparation for a future, more significant campaign to create a validation database for NIRSS. This paper focuses on the later objective, outlining the analysis methods and tools in detail and concluding with several case studies from balloon releases in March 2014.

2.0 Background Information

2.1 NIRSS

The NIRSS combines the data from several vertically-pointing, meteorological instruments to generate an icing hazard product. The system instruments include a Radiometrics Corporation TP/WVP-3000 radiometer, a Vaisala CT25K Ceilometer and a METEK Meteorologische Messtechnik GmbH MIRA36 Ka-Band Cloud Radar System.

The Radiometrics microwave radiometer is capable of deriving integrated liquid water (ILW), temperature and humidity profiles by measuring a cone of the atmosphere that originates at the microware receiver, and ranges from 4° and 6° beam widths, based on frequency. Temperature profiles are obtained by measuring the brightness temperature (radiation intensity) in the 60 GHz frequency range. The emission of oxygen is proportional to temperature and density, allowing temperature profiles to be derived. The water vapor profiles are obtained in the 22 GHz range. The radiation intensity of water vapor is proportional to vapor density and temperature, allowing the vapor profiles to be derived. The cloud liquid water emission spectrum has no resonance frequency, so the full instrument measurement frequency range is utilized. The radiometer uses a neural network developed from radiosonde soundings to determine the upper atmospheric data. The Vaisala ceilometer is a vertically pointing pulsed diode laser that sends out short laser pulses vertically, and measures the backscatter to determine the cloud base for the NIRSS algorithms. Finally, the METEK Ka-Band is a vertically-pointing radar used to define the cloud top and cloud base altitudes.

At the time of the March 2014 balloon releases, the NIRSS was vertically pointing only. It has since been expanded to provide volumetric coverage of icing conditions in the terminal area. The system utilizes a slant elevation radiometer and NEXRAD radar data in addition to the NIRSS instrumentation used for the data collection presented in this paper. Further detail on the terminal area system is provided in Reference 1.

2.2 Balloon-Borne, In-situ Instrument Package

2.2.1 Instrument Package

The instrument package (Fig. 1) included the iMet-1-RSB Radiosonde and the Anasphere SLWC sensor. The iMet-1-RSB is a meteorological radiosonde designed to transmit upper air pressure, temperature, humidity, and GPS data on the 403 MHz meteorological frequency once every second. It is capable of interfacing and transmitting the data acquired by additional third party sensors; this capability was used to obtain the SLWC measurements from the Anasphere SLWC sensor. The principle behind the vibrating wire sensor is the change in natural frequency of a wire due to ice accretion on the wire. The natural frequency of the wire decreases as ice accretes. Profiles of SLWC can be derived from the time history of the measured wire vibration frequency and ascent rate.

Atek Data Corporation was the original developer of the vibrating wire sensor for measuring SLWC (Refs. 2 to 4). Anasphere, Inc. produced a new prototype sensor through NASA sponsored Small Business Innovative Research (SBIR) contracts starting in 2012, building upon the Atek concept. The Anasphere design focused on improving performance, power consumption, integrating radiosonde capability and reducing size and weight. The wire element is periodically “plucked” using a servomotor with a magnet attached to a short arm. A piezoelectric sensor measures the wire vibration frequency, and the natural frequency is determined every 3 sec, nominally. The Anasphere second generation sensors had an expected vibrational plane parallel with the freestream to maintain consistency with the Atek development work. Reference 5 describes the SLWC Sensor in greater detail and includes case studies with the sensor conducted in Boulder, Colorado in 2012.

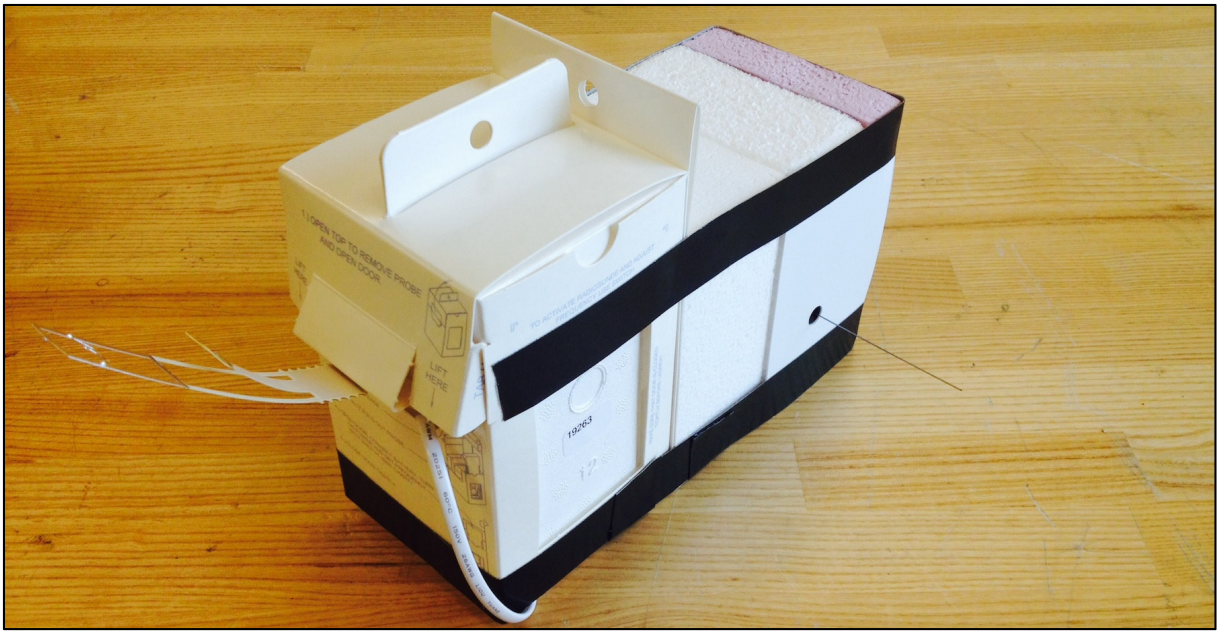

Figure 1.—iMet-1-RSB radiosonde and anasphere SLWC probe combined instrument package used in 2014.

Soundings from radiosondes are generally regarded as defining the atmosphere at an instant in time and space, specifically, the time and location of release, despite the true ascent time and spatial translation, due to prevailing winds, from the release point. In contrast to the NIRSS, the balloon-borne instruments only sample the local conditions in proximity to the instrument package. Thus, the NIRSS and radiosonde data have notably different spatial and temporal resolutions that should be noted.

2.2.2 Ground Station Sounding System

The ground station used was the International Met Systems, Inc. (InterMet) iMet-3150 403 MHz Sounding System; an automated sounding system that acquires and stores data without need for user input after balloon release. The system uses the ICOM IC-R20 Receiver and InterMet iMet Radiosonde Decoder to collect, decode and send the telemetry by the iMet-1-RSB to the Skysonde software package, where the data is collected, stored and used to generate automated reports for the user.

The Skysonde software package is a product of the Cooperative Institute for Research in Environment Sciences. A modified version of Skysonde that accepts external sensor data from the InterMet iMet-1-RSB radiosondes via the XDATA protocol was used, which allowed researchers to acquire data from the Anasphere SLWC sensor.

3.0 Data Reduction Process

The data from the first radiosonde release from March 1, 2014 was used to illustrate the data reduction process, from the raw data to the final results, in the following subsections.

3.1 Raw Data

The raw sounding data saved to file by the Skysonde software package during flight was filtered prior to data reduction. The iMet-1-RSB transmits pressure, temperature, relative humidity and GPS telemetry once a second, but only transmits XDATA when the SLWC sensor reports new frequency data. This occurs once every 3 sec. Thus the data has 15 m vertical spatial resolution, assuming a nominal ascent rate of 5 m/s. The data file was filtered to extract only XDATA telemetry entries corresponding to new frequency measurements, as Skysonde fills null fields with the most recent valid entry.

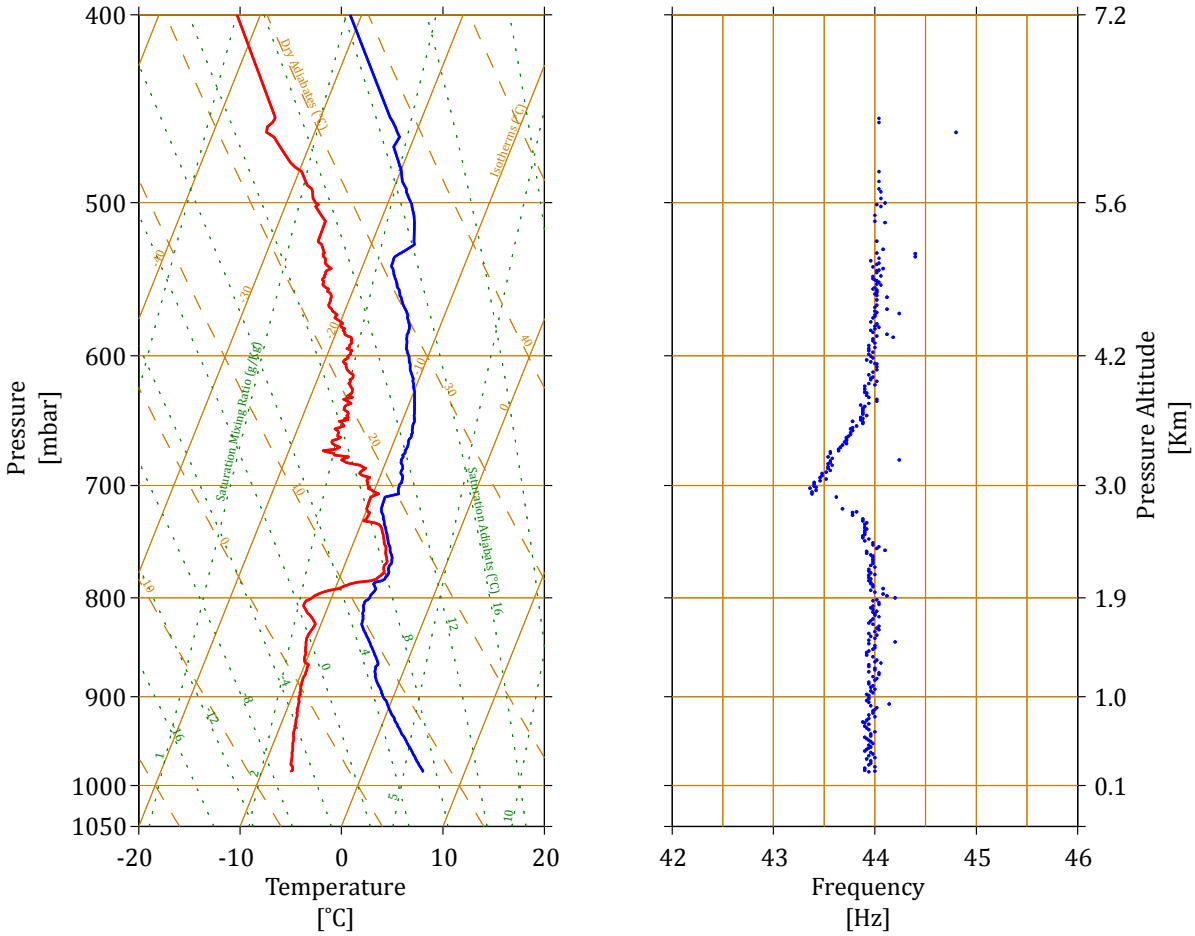

Figure 2.—March 01, 2014 Release 01 raw data; (left) skew-T, Log-P Diagram showing temperature (blue) and dew point (red), and (right) the corresponding SLWC sensor frequency telemetry.

Figure 2 shows the Skew-T, Log-P plot alongside the raw frequency telemetry from the first March 1, 2014 launch. The Skew-T, Log-P plot on the left shows the temperature in blue and the dew point in red. The presence of cloud is indicated at altitudes where the dew point depression decreases between 2 and 3 Km. The nominal 44 Hz natural frequency and characteristic frequency depression due to ice accretion are readily observed in the right plot. The frequency depression starts towards the center of the cloud layer, maximizing near the cloud top, as indicated by the Skew-T, Log-P plot. The frequency slowly increases upon the radiosonde exiting the cloud top and returns to the nominal value.

3.2 Outliers and Piecewise Averaging

Evident outliers in the frequency data were removed prior to data reduction using minimum and maximum threshold values of 40 and 48 Hz, respectively. Several additional outliers in the frequency data are apparent in Figure 2. To systematically handle these outliers, several sensors were tested to estimate a general measurement precision, and a piecewise average trend was developed to evaluate telemetry for exclusion.

Ten second generation SLWC Sensors were bench tested to provide a basis for a general estimate of the measurement precision. Each sensor was tested for 30 min, yielding 600 frequency measurements, in two different configurations; clamped to the bench and suspended with string. The sensors were powered by a DC power supply during the tests to ensure consistent power levels. The resulting mean values and standard deviations are 44.49 and 0.026 Hz and 44.71 and 0.021 Hz for the clamped and suspended tests, respectively.

The piecewise average trend was developed using an averaging interval of 30 sec. The data corresponding to the minimum recorded frequency during a sounding was maintained as a distinct data point to preserve the shape of the frequency depression. Data that did not fall within ±0.1 Hz of the piecewise average trend was marked and excluded from the analysis. The ±0.1 Hz threshold is slightly greater than three standard deviations from the bench testing, and is the estimate of the measurement precision used to analyze the telemetry from the SLWC Sensor for this effort. The process was repeated iteratively, removing only a single outlier each cycle and redeveloping the piecewise trend until all data fell within the defined threshold. Figure 3 shows the final piecewise average trend and the outliers in the frequency telemetry.

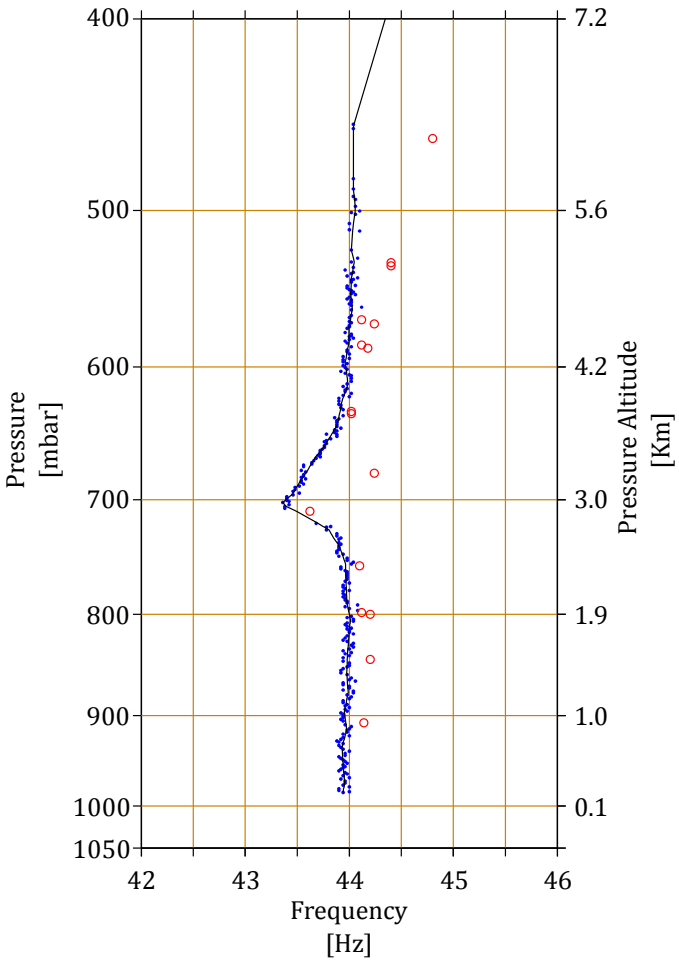

Figure 3.—March 01, 2014 Release 01 frequency data; frequency data (blue dots), frequency data outliers (red circles), and piecewise averaging trend line (black line).

3.3 Calculation of the Frequency Derivative

The frequency time derivative, df/dt, is the most significant term in the calculation of SLWC. Inherent noise in the raw frequency data, and thus the frequency time derivative, tends to cause the resulting SLWC profile to appear noisy, even non-physical. Reference 5 used an 11 point span moving average to smooth the frequency data from SLWC Sensors released from Boulder, Colorado in March 2012, and demonstrated good agreement between the smoothing model and the raw data. However, the moving average did not perform as well with the frequency data obtained from March 2014 releases of SLWC sensors from NASA Glenn Research Center. Thus, several smoothing models were examined to determine an appropriate method to smooth the frequency data to address the noise.

The smoothing models examined included a moving average filter with coefficients equal to the reciprocal of the user defined span, a robust local regression using weighted linear least squares and a first degree polynomial (LOWESS) or a second degree polynomial (LOESS), and a Savitzky-Golay filter. The robust LOWESS and LOESS smoothing models assign lower weight to algorithm-determined outliers. All of these smoothing models are native to the MATLAB (The Mathworks, Inc., Natick, MA) Curve Fitting Toolbox. Figure 4 shows the smoothing models applied to the frequency data from the first release on March 01, 2014 with varying spans. Upon visual inspection, the LOESS model follows the data trend better than the other methods, and is relatively insensitive to the defined span. Moving average, LOWESS and Savitzky-Golay are more sensitive to the span selection, and do not capture the trend of the frequency depression as well. Thus, the LOESS model was selected to smooth the data.

A generalized central differencing method, Equation (1), was used to obtain the frequency time derivative as the time between frequency measurements varies due to possible data dropouts and the elimination of outliers.

$$\left(\frac{df}{dt}\right)_i = \frac{1}{2}\left[\frac{f(t_{i+1}) - f(t_i)}{t_{i+1} - t_i} + \frac{f(t_i) - f(t_{i-1})}{t_i - t_{i-1}}\right] \tag{1}$$

The term i in Equation (1) is the index of the smoothed frequency data.

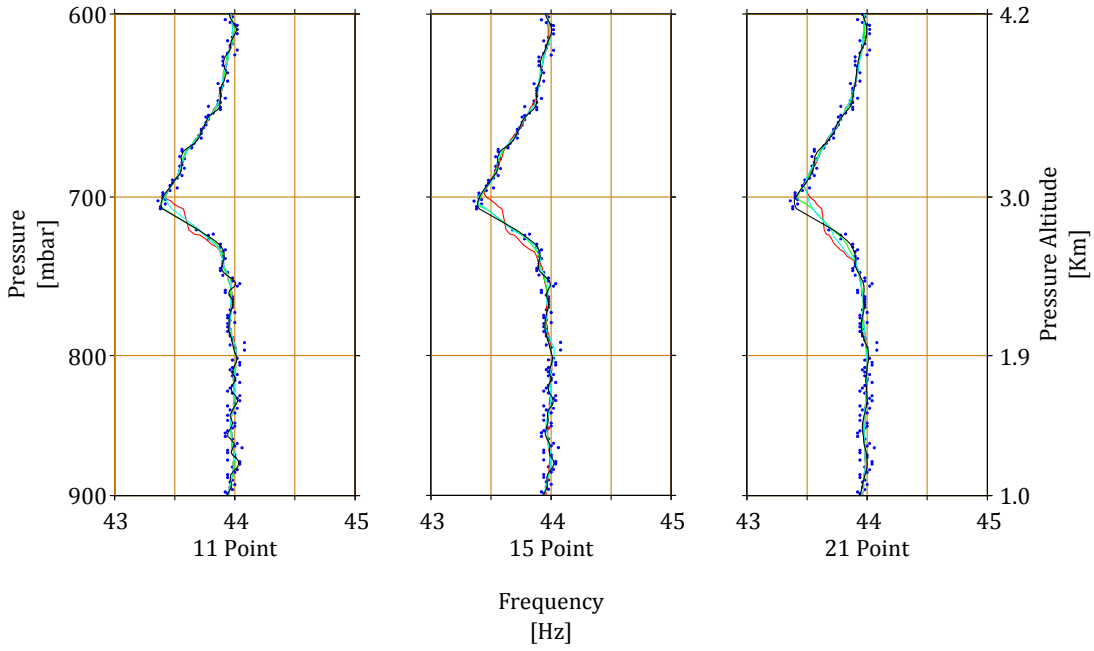

Figure 4.—March 01, 2014 Release 01 Smoothing Model Comparison; frequency data (blue dots), moving average (red line), robust LOWESS (green line), robust LOESS (black line) and Savitzky-Golay filter (cyan line).

3.4 Supercooled Liquid Water Content

The supercooled liquid water content calculation was originally to be calculated as described by the model in Reference 4. However, it was discovered post test that the SLWC Sensors released during March 2014 were orientated such that the wire vibration planes were not vertical, nominally aligned with the freestream direction, but were instead rotated such that the vibration planes were horizontal, orthogonal with the freestream direction. Thus, this initiated further investigation of the model published in References 2 to 4 to ensure the fidelity of the final results. The following subsections examine the model published by the original developer, re-deriving the equations in a more generalized form than presented in References 2 to 4 in order to expand the model to include equations to determine SLWC for an element oriented orthogonally to the freestream flow without neglecting the effect of ice stiffness. The method used to determine collection efficiency is also included. Finally, a comparison between the two models is presented, along with application of both models to the first release from March 01, 2014.

3.4.1 Supercooled Liquid Water Content Neglecting Ice Stiffness

The method described in Reference 4 is used to calculate the SLWC neglecting the effects of ice stiffness. The derivation for Reference 4 equations is shown in this document to provide the generalized forms that do not reference specific lengths for L_0 and L_1, which are illustrated in Figure 5, to address a discrepancy in the equation to calculate SLWC published in Reference 4, and provide a basis for the derivation of a model for the March 2014 winter soundings presented in this work. The ice distribution shown in Figure 5 is idealized, and does not take into account the effect of the instrument chassis or the varying orientation of the instrument chassis relative to the freestream flow on the shape of the distribution. The potential energy, PE, and kinetic energy, KE, of a vibrating wire loaded with ice are described by Equations (2) and (3), where E, I and M are the modulus of elasticity, bending moment of inertia and mass per unit length, respectively. The subscripts i and w are used throughout this document to designate the ice and the wire.

$$PE = \frac{E_w I_w}{2} \int_0^{L_0} \left(\frac{\partial^2 y}{\partial x^2}\right)^2 dx + \frac{E_i I_i}{2} \int_{L_1}^{L_0} \left(\frac{\partial^2 y}{\partial x^2}\right)^2 dx \tag{2}$$

$$KE = \frac{M_w}{2} \int_0^{L_0} \left(\frac{\partial y}{\partial t}\right)^2 dx + \frac{M_i}{2} \int_{L_1}^{L_0} \left(\frac{\partial y}{\partial t}\right)^2 dx \tag{3}$$

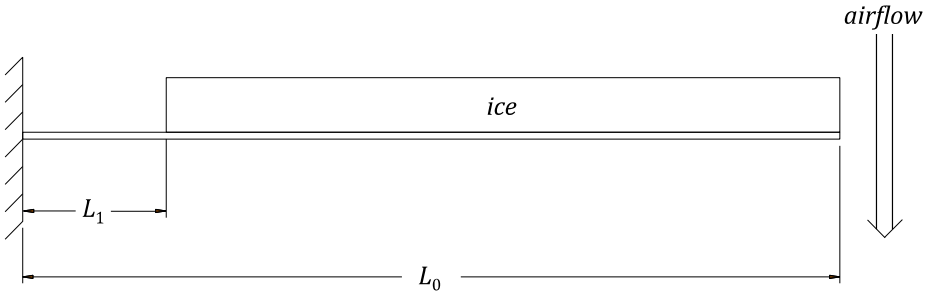

Figure 5.—Illustration of wire and ice load (reproduced from Ref. 4).

The displacement of the wire is described by Equation (4), where B is an unspecified amplitude and f is the wire vibration frequency.

$$y = B\left[cos\left(\frac{\pi x}{2L_0}\right) - 1\right] cos(2\pi ft) \tag{4}$$

Equations (5) and (6) are the bending moments of inertia with respect to the horizontal axis for the rime-like ice geometry shown in Figure 6(a) and used by Reference 4, though not explicitly illustrated in Reference 4. These terms can be obtained using the procedures outlined in Reference 6.

$$I_w = \frac{\pi}{64} D^4 \tag{5}$$

$$I_i = D^4\left(\frac{\alpha^3}{3} + \frac{\alpha^2}{2} + \frac{\alpha}{4}\right) \tag{6}$$

The generalized form of equation derived in Reference 4, Equation (7), is obtained by evaluating Equations (2) and (3) using Equation (4), setting the resulting $cos(2\pi ft)$ and $sin(2\pi ft)$ terms equal to unity for maximum energy, and solving for the vibration frequency, f. The result is

$$f^2 = \frac{\pi^2 E_w \left\{I_w + \frac{1}{\beta}\left[\left(1 - \frac{L_i}{L_0}\right) - \frac{1}{\pi} sin\left(\frac{\pi L_1}{L_0}\right)\right] I_i\right\}}{128 L_0^4 \left\{\left(\frac{3\pi - 8}{2\pi}\right) M_w + \frac{1}{2\pi}\left[8sin\left(\frac{\pi L_1}{2L_0}\right) - sin\left(\frac{\pi L_1}{L_0}\right) + 3\pi\left(1 - \frac{L_1}{L_0}\right) - 8\right] M_i\right\}} \tag{7}$$

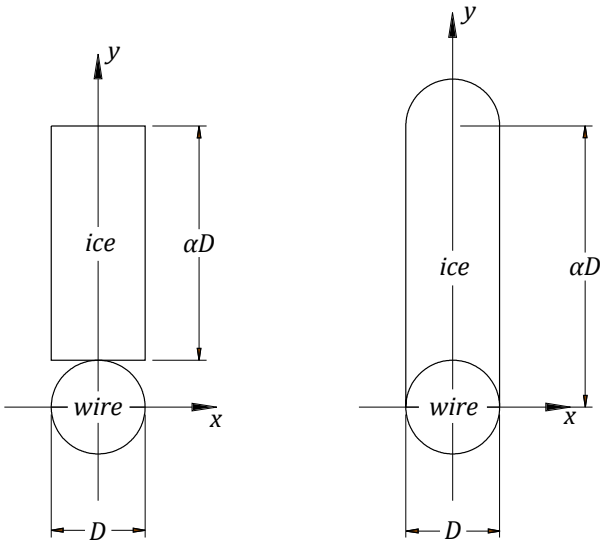

Figure 6.—Idealized cross sections of accreted ice on wire. (a) The cross section assumed by Reference (4) to obtain Equations (5) and (6), and (b) the cross section assumed in Section 3.4.2 to obtain Equations (19) and (20).

where

$$\beta = \frac{E_w}{E_i}. \tag{8}$$

By defining the coefficients c_1, c_2 and c_3 as shown in Equations (9) to (11), Equation (7) can be simplified and written as shown by Equation (12). The values for the coefficients c_1, c_2 and c_3 match those reported in Reference 4 using the lengths L_0 and L_1 defined in Reference 2.

$$c_1 = \left(1 - \frac{L_1}{L_0}\right) - \frac{1}{\pi} sin\left(\frac{\pi L_1}{L_0}\right) \tag{9}$$

$$c_2 = \left(\frac{3\pi - 8}{2\pi}\right) \tag{10}$$

$$c_3 = \frac{1}{2\pi}\left[8sin\left(\frac{\pi L_1}{2L_0}\right) - sin\left(\frac{\pi L_1}{L_0}\right) + 3\pi\left(1 - \frac{L_1}{L_0}\right) - 8\right] \tag{11}$$

$$f^2 = \frac{\pi^2 E_w \left(I_w + \frac{c_1}{\beta} I_i\right)}{128 L_0^4 (c_2 M_w + c_3 M_i)} \tag{12}$$

The vibration frequency of the wire is the natural vibration frequency of the wire, f_0, when no ice is present on the wire. Equation (14) is the result.

$$M_i = 0 \ \rightarrow f = f_0 \tag{13}$$

$$f_0^2 = \frac{\pi^2 E_w I_w}{128 L_0^4 c_2 M_w} \tag{14}$$

Equation (15), the time-rate of change of the ice mass per unit length, is obtained by introducing Equations (14) into (12), and differentiating with respect to time.

$$\frac{dM_i}{dt} = -\frac{2c_2 M_w f_0^2}{c_3 f^3} \frac{df}{dt} \tag{15}$$

It is important to note that Reference 4 treats the bending moment of inertia of the ice, I_i, as a constant, citing negligible ice stiffness (Refs. 2 and 4). Reference 4 postulates low velocity drop impingement on the wire leads to the formation of a "soft rime," citing that there is no evidence of ice stiffness effect apparent in the results of laboratory testing published in Reference 3. Reference 4 states that tension produces cracks and compression produces irreversible compressions in the ice during the vibration cycle, citing Reference 7. Reference 4 postulates that these cracks and compressions may "contribute to the absence of stiffness effects."

The SLWC is defined by Equation (16) (Ref. 4). The terms ε and ω are the collection efficiency of the wire and ascent rate of the weather balloon, respectively. Combining Equations (15) and (16), and defining the coefficient b, shown by Equation (17), the SLWC can be calculated using Equation (18).

$$\text{SLWC} = \frac{1}{\varepsilon D \omega} \frac{dM_i}{dt} \tag{16}$$

$$b = \frac{c_2}{c_3} M_w \tag{17}$$

$$\text{SLWC} = -\frac{2bf_0^2}{\varepsilon D \omega f^3} \frac{df}{dt} \tag{18}$$

Equation (18) does not have the unit discrepancy present in the Reference 4 equation for SLWC. This equation assumes that the stiffness of the accreted ice has a negligible effect on the wire vibration frequency depression. Only the mass of accreted ice affects the frequency depression according to Equation (18). The development of Equation (18) thus assumes that the orientation of the wire vibrational plane and the accreted ice have no effect on the frequency depression.

3.4.2 Supercooled Liquid Water Content Considering Ice Stiffness

This section will examine the SLWC calculation for a wire vibrating orthogonal to the freestream flow direction without neglecting the effects of ice stiffness. The ice stiffness is not considered negligible in this model, setting aside the "soft rime" ice postulated in Reference 4. Equation (19) is the bending moment of inertia for the Figure 6(b) about the horizontal axis. It has been included for completeness, but it is directly not applicable to the March 2014 cases discussed in this work. The bending moment of inertia of the ice for the rime-like geometry shown in Figure 6(b) about the vertical axis is provided in Equation (20), and the mass of ice per unit length is given by Equation (21), where ρ_i is the density of the ice. A value of 870 kg/m^3 is assumed to be an appropriate estimate for the density for the analysis, based on the results from Reference 8. The expression for the bending moment of inertia as a function of the mass per unit length of ice, Equation (22), is obtained by combining Equations (20) and (21).

$$I_{i_x} = D^4 \left(\frac{\pi \alpha^2}{8} + \frac{\alpha^3}{3} \right) \tag{19}$$

$$I_{i_y} = \frac{1}{12} \alpha D^4 \tag{20}$$

$$M_i = \rho_i \alpha D^2 \tag{21}$$

$$I_{i_y} = \frac{D^2}{12\rho_i} M_i \tag{22}$$

Equations (12) and (22) combine to provide Equation (23) that relates the mass of accreted ice per unit length to the vibrating frequency of the wire. The term b is as previously defined, and σ is given by Equation (24).

$$M_i = \frac{I_w \left(\frac{f^2}{f_0^2} - 1 \right)}{\frac{c_1}{\beta} \sigma - \frac{I_w f^2}{b f_0^2}} \tag{23}$$

$$\sigma = \frac{D^2}{12\rho_i} \tag{24}$$

Equation (25) is the time derivative of the mass per unit length, dM_i/dt. Combining Equations (16) and (23) gives Equation (26), which does not assume that the stiffness of the accreted ice is negligible for a wire with a vibrating plane perpendicular to the free stream flow.

$$\frac{dM_i}{dt} = \frac{2bI_w\beta f_0^2 f(c_1 b\sigma - \beta I_w)}{(c_1 b\sigma f_0^2 - \beta I_w f^2)^2}\frac{df}{dt} \tag{25}$$

$$\text{SLWC} = \frac{2bI_w\beta f_0^2 f(c_1 b\sigma - \beta I_w)}{\varepsilon D\omega(c_1 b\sigma f_0^2 - \beta I_w f^2)^2}\frac{df}{dt} \tag{26}$$

Equation (26) assumes the plane of vibration of the wire is orthogonal to the freestream flow direction and a rime-like ice accretion along the wire. Additionally, both Equations (18) and (26) assume a uniform accretion along the wire as shown in Figure 5.

3.4.3 Collection Efficiency

The collection efficiency is determined using the methods outlined in References 9 and 10, where the dimensionless inertial parameter, K, given by Equation (27), and a dimensionless parameter, φ, given by Equation (28), are used to develop a collection efficiency curve based on drop size.

$$K = \frac{\rho_l d^2 u}{9\mu D} \tag{27}$$

$$\varphi = \frac{9\rho_a^2 D u}{\mu\rho_w} \tag{28}$$

The terms u, d, μ and ρ are the speed, drop diameter, the dynamic viscosity and the density, respectively. The subscripts a and l denote the air and the supercooled liquid water. It should be noted that the term ω for ascent rate is equivalent to the term u for this method. The radiosonde rises at a nominal rate of 5 m/s, giving a $\varphi \approx 2.5$, assuming thermodynamic properties at 0 °C. The resulting collection efficiency curves for several ascent rates are shown in Figure 7. The difference between the 3 and 7 m/s curves are 17, 8, and 4 percent at 10, 15, and 20 µm, respectively.

The collection efficiency calculation presented takes only the clean wire into account. The effect of the SLWC sensor package is not considered, the package orientation to the freestream flow is idealized and the effect of ice accretion is neglected. Reference 5, which describes SLWC sensor field tests from 2012, uses the methods described in Reference 11 to determine collection for an unheated, nonrotating cylinder.

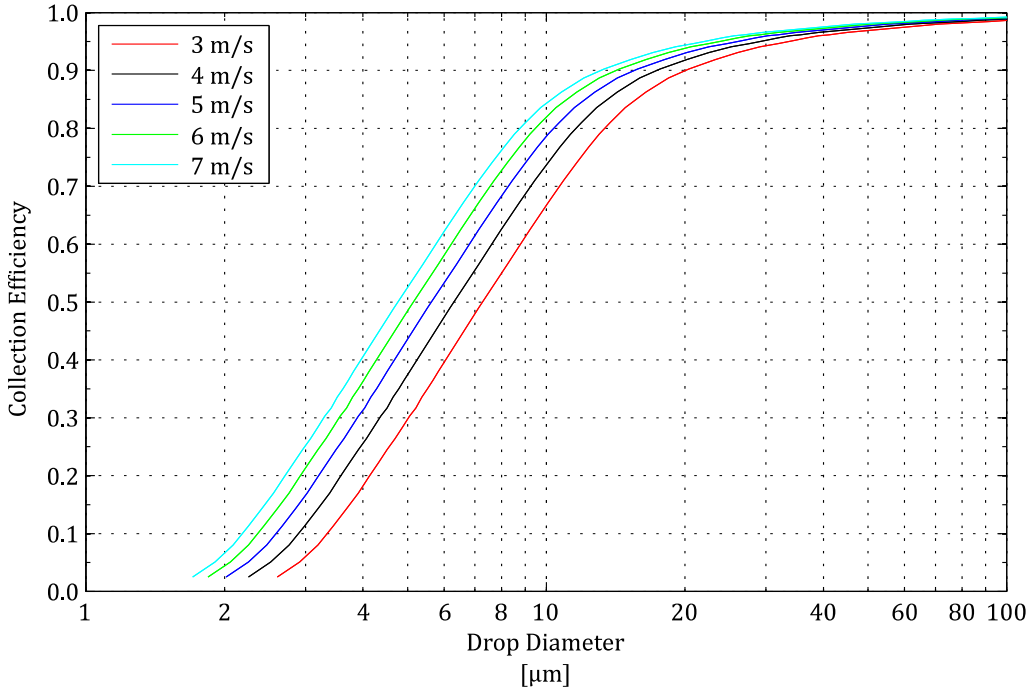

Figure 7.—Collection efficiency for a 0.6 mm diameter wire at several speeds. Assumed 0 °C to estimate thermodynamic properties, and used the methods defined in Reference 9.

3.4.4 SLWC Model Comparison

Both SLWC Equations (18) and (26) have the form expressed by Equation (29), where the coefficient, C, is defined by C_H, Equation (30), for Equation (18), and by C_K, Equation (31), for Equation (26). Figure 8 shows the two coefficients plotted together and Figure 9 shows the ratio of C_K/C_H, plotted as a function of wire vibrational frequency. It is worth reiterating that the natural vibrational frequency of the wire decreases with increasing ice accretion, thus the horizontal axes are reversed for both Figures 8 and 9 to aid the reader.

$$\text{SLWC} = \frac{C}{\varepsilon D \omega}\frac{df}{dt} \tag{29}$$

$$C_H = -\frac{2bf_0^2}{f^3} \tag{30}$$

$$C_K = \frac{2bI_w\beta f_0^2 f(c_1 b\sigma - \beta I_w)}{(c_1 b\sigma f_0^2 - \beta I_w f^2)^2} \tag{31}$$

A slight difference between the models exists at the assumed natural frequency of 44 Hz for a clean wire, which was used to develop Figures 8 and 9, where the absolute magnitude of C_K is approximately 10 percent larger than C_H. This difference is a result of the assumptions used to derive each model. The value of C_K approaches C_H when the modulus elasticity of ice, E_i, is parametrically reduced such that the term β increases. Reducing the modulus of elasticity of ice in this manner effectively leads to a model where the stiffness of the ice is neglected, as it is in References 2 to 4. The result is two essentially equivalent models. Finally, examination of Figure 9 shows the difference between the two models increases with decreasing frequency, up to approximately 26 percent at 35 Hz, suggesting the effect of stiffness may not be negligible when the sensor is exposed to conditions that lead to significant icing upon the wire.

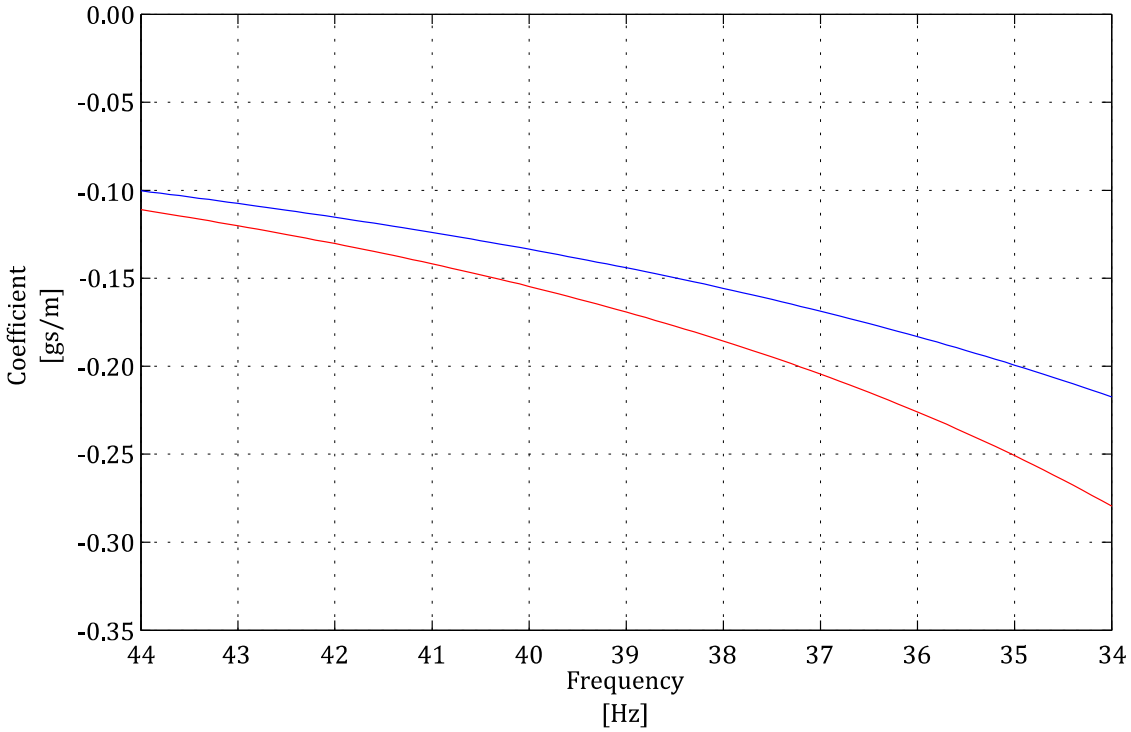

Figure 8.—Comparison between the Equation (18) coefficient, Equation (30), (blue) and the Equation (26) coefficient, Equation (31), (red) as a function of frequency.

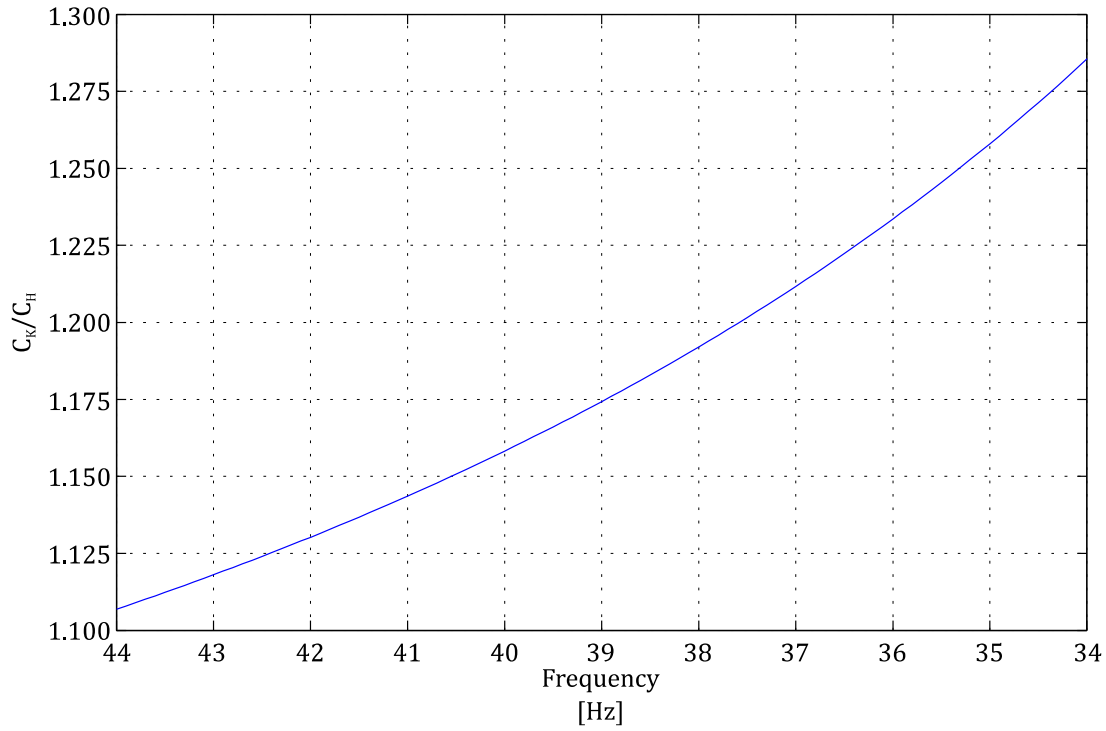

Figure 9.—Ratio of the Equation (26) coefficient, Equation (31), to the Equation (18) coefficient, Equation (30).

3.4.5 SLWC Calculation

Figure 10 shows the final supercooled liquid water result from the March 1, 2014 sounding using both models. The calculations were carried out assuming a median volumetric diameter (MVD) of 15 µm as in-situ measurement of MVD was unavailable. The estimated collection efficiencies at a nominal ascent rate of 5 m/s for 10, 15 and 20 µm are 0.8, 0.89, and 0.93, respectively. Lower collection efficiency drives the calculated SLWC higher. The vertical profiles obtained from Equations (18) and (26) agree. The calculated SLWC from Equation (26) tends to be higher than Equation (18). A filter requiring the in-situ relative humidity to exceed 75 percent was also used to filter out any additional variation in the calculated SLWC.

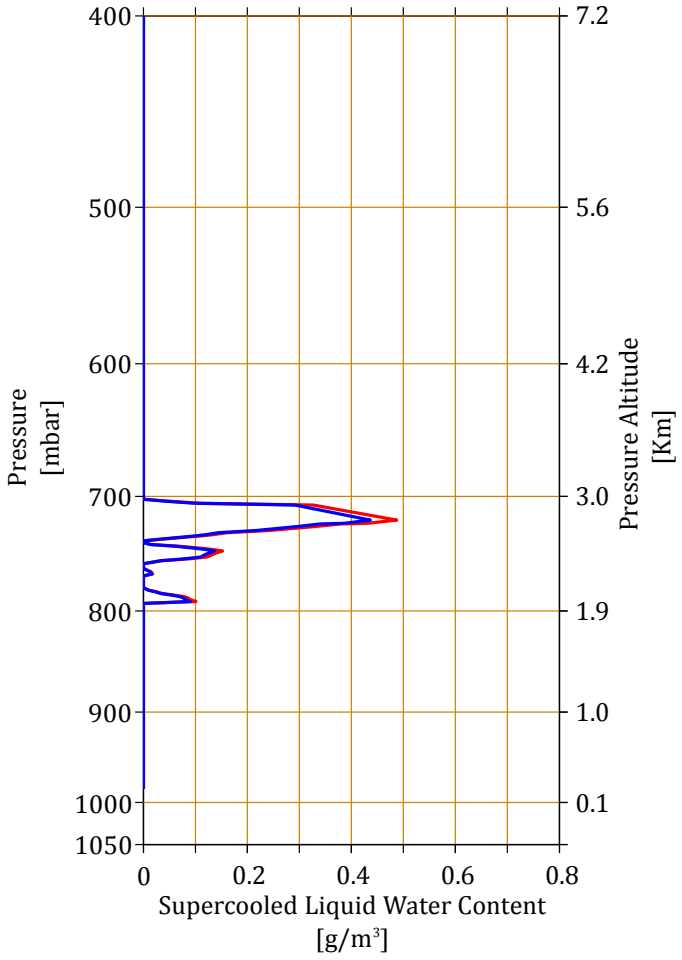

Figure 10.—March 01, 2014 Release 01 SLWC comparison; Equation (18) (blue) and Equation (26) (red).

3.5 Integrated Liquid Water Content

The NIRSS uses the radiometer-derived integrated liquid water (ILW), an integrated measure of the amount of liquid in a vertical column above the instrument, to develop the vertical LWC profile. The ILW provides a point of comparison between the ground-based remote sensor measurements and the balloon-derived in-situ data. The ILW, provided a known LWC profile, is given by

$$\mathrm{ILW} = \frac{1}{\rho_{(H_2O)liq}} \int_{z_0}^{z} \mathrm{LWC}\, dz. \tag{32}$$

Equation (34), which is obtained by introducing Equation (33) into Equation (32), is used to calculate the ILW from the balloon data. It should be noted that the SLWC sensor only measures SLWC, and the final NIRSS product only accounts for the supercooled fraction of the integrated liquid derived by the radiometer. Thus, the LWC terms defined in Equations (32) and (34) are actually the SLWC profiles, and the ILW is more accurately defined as the supercooled integrated liquid water, for the purposes of this document.

$$dz = \omega\, dt. \tag{33}$$

$$\mathrm{ILW}_B = \frac{1}{\rho_{(H_2O)liq}} \int_{t_0}^{t} \mathrm{LWC}\, \omega\, dt \tag{34}$$

3.6 NIRSS Code Error and Liquid Water Content Profile Scaling

A difference between the radiometer ILW and the NIRSS ILW, calculated from the NIRSS SLWC profile, was discovered through the course of this research. The difference in the values was traced to an error in the NIRSS code, which was not identified and corrected at the time of completion of this document. Thus, the NIRSS SLWC profile was corrected by scaling the data using Equation (35), where the superscripts S and O represent the scaled and the original NIRSS output, respectively, and i denotes the index of a given SLWC value in the vertical profile.

$$\mathrm{SLWC}_i^S = \frac{\mathrm{ILW}_{3005}}{\mathrm{ILW}_{NIRSS}^O} \mathrm{SLWC}_i^O \tag{35}$$

Figure 11 shows the difference between the original and scaled NIRSS profiles. The ILW calculated from the original NIRSS output was 0.06 mm, where the radiometer-derived ILW was 0.26 mm. After applying Equation (35), the resulting ILW calculated from the scaled profile matches the radiometer ILW. The scaled profile is the expected output from NIRSS for this sounding (D. Serke, personal communication, 2015). It should be noted that the scaling factor varied for each sounding, and the NIRSS SLWC profiles throughout the rest of this document have been scaled to correct for this error.

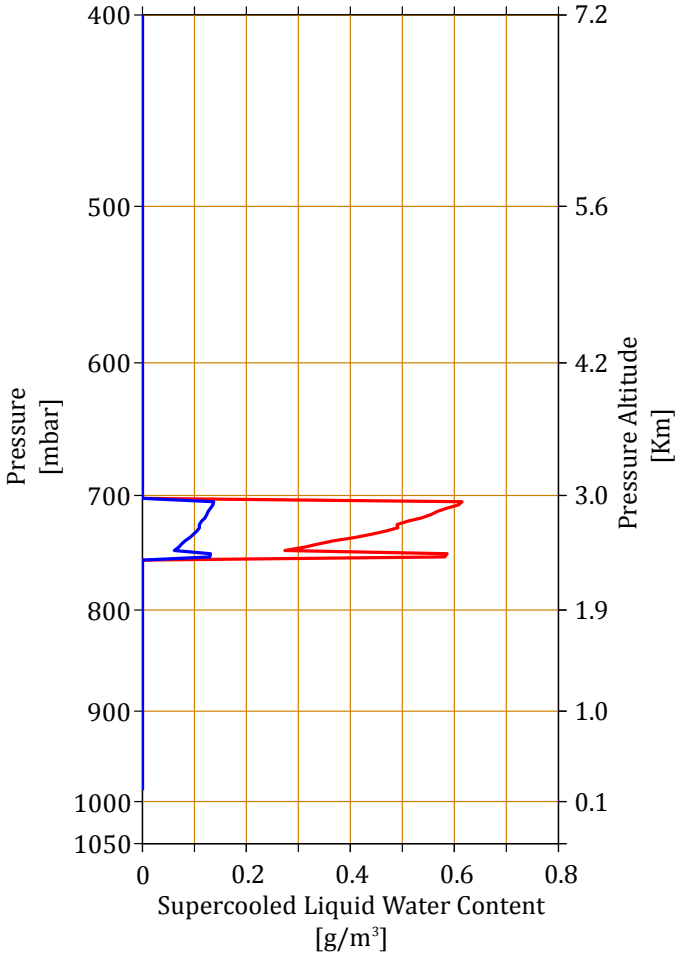

Figure 11.—March 01, 2014 20:14 UTC NIRSS Liquid Water Content Profile; original NIRSS output (blue), scaled NIRSS output using Equation (35) (red).

4.0 Final Data and Analysis

Five radiosondes were released in March 2014 during two separate icing events on March 1 and March 8. The following sections compare the final data from the NIRSS and the radiosondes. Based on the temporal and spatial resolutions between the NIRSS and radiosondes, it has been assumed that the icing conditions aloft are synoptic conditions that vary slowly in time, forming the basis of comparison between the remote sensing and in-situ instrumentation in this research.

4.1 March 1, 2014 Soundings

Two instrument packages were released on March 1, 2014. The first release (20140301-001) occurred at 20:14 UTC and the second (20140301-002) at 21:06 UTC. Figures 12 and 13 show the reduced data from the instrument packages 20140301-001 and 20140301-002, respectively, with comparison to the NIRSS profile output. The left plots are the Skew-T, Log-P comparison diagrams and the right plots are the comparison between the SLWC calculated by NIRSS and SLWC calculated from the radiosonde data using Equation (26).

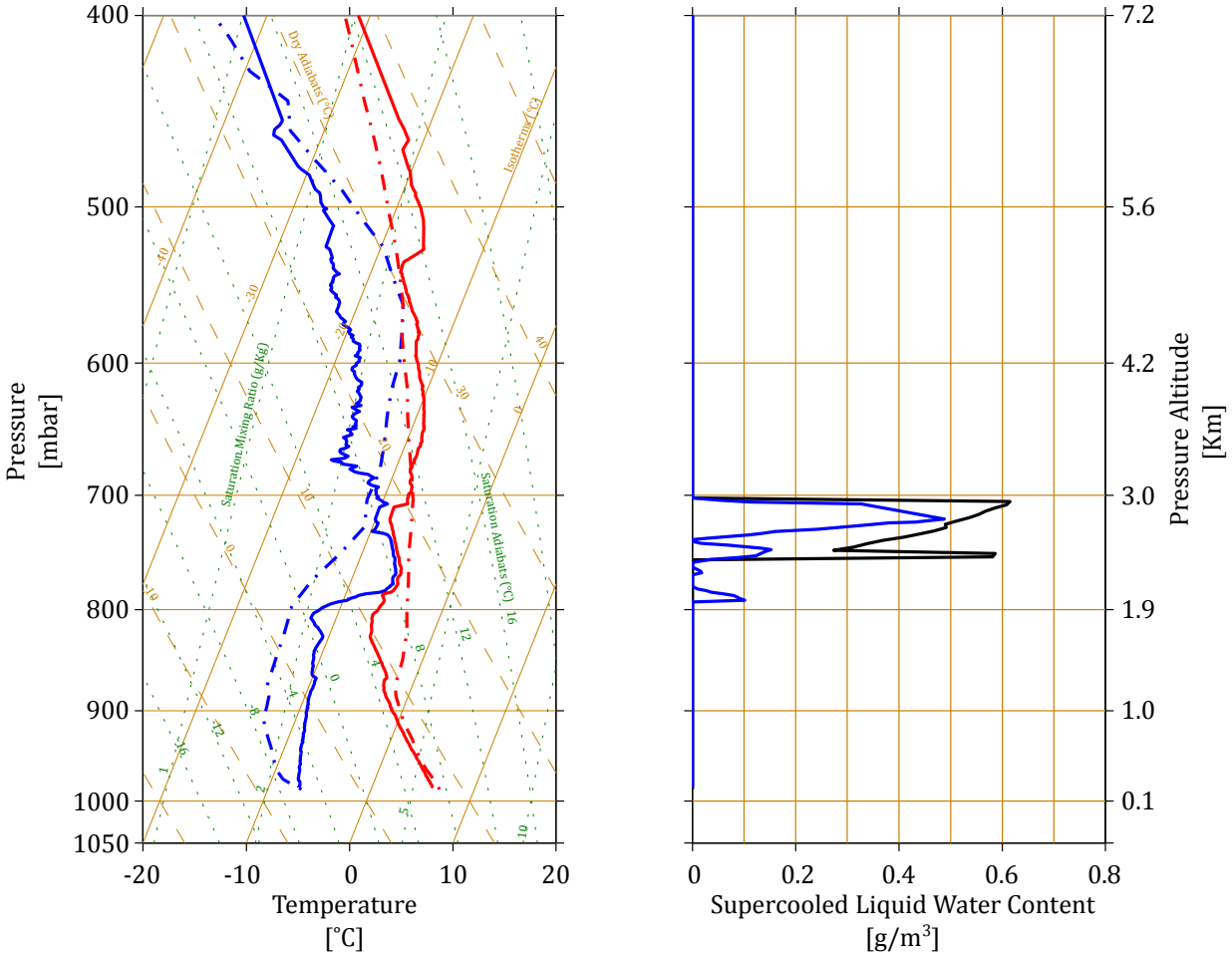

Figure 12.—March 01, 2014 Release 01 Final Data; (left) Skew-T, Log-P Diagram showing temperature (red) and dew point (blue) for the instrument package (solid) and NIRSS (dashed), and (right) the corresponding, calculated SLWC from Equation (26) (blue) and NIRSS (black).

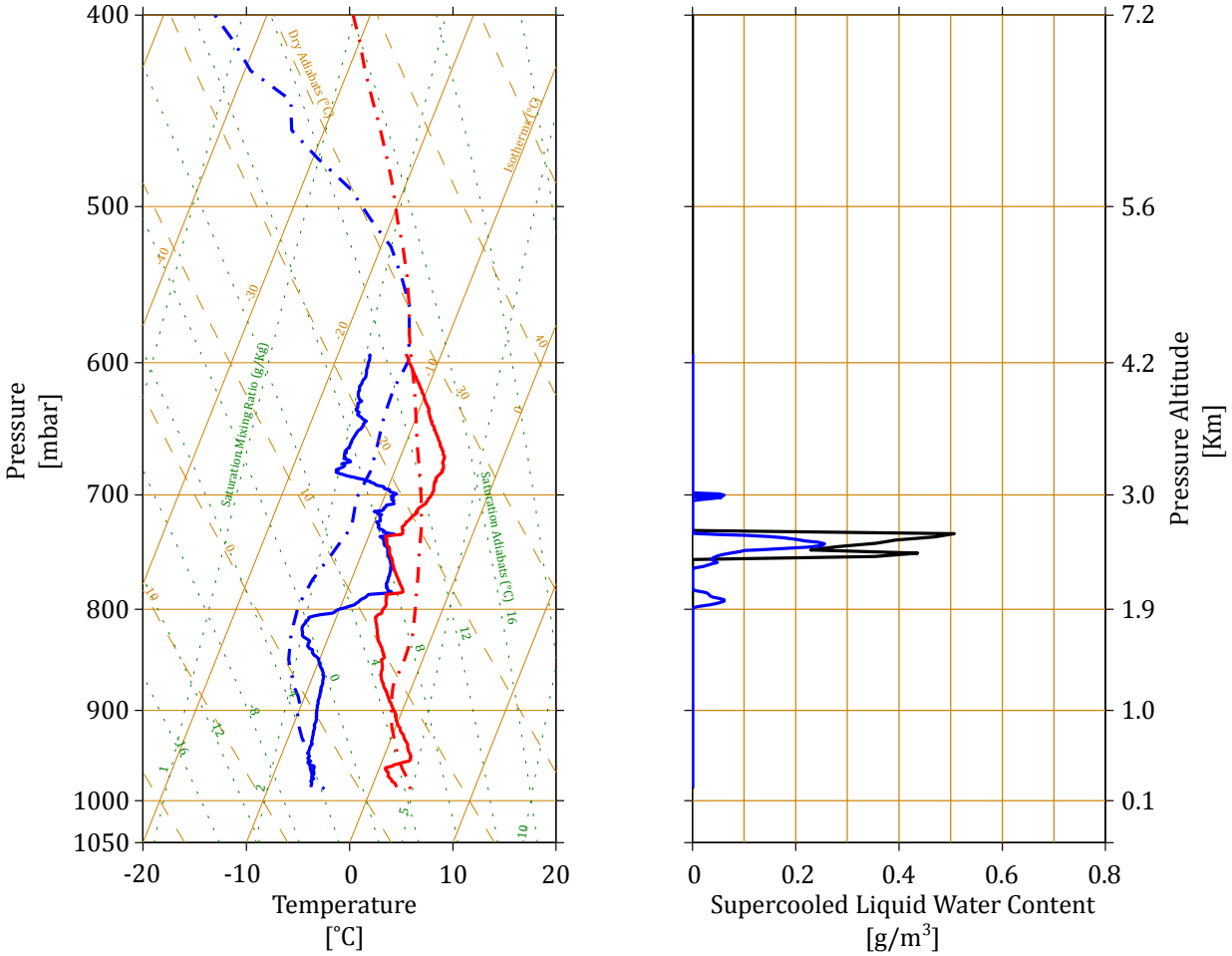

Figure 13.—March 01, 2014 Release 02 Final Data; (left) Skew-T, Log-P Diagram showing temperature (red) and dew point (blue) for the instrument package (solid) and NIRSS (dashed), and (right) the corresponding, calculated SLWC from Equation (26) (blue) and NIRSS (black).

The 20140301-001 package indicated cloud base at an altitude of 2 Km, well above the freezing layer, just below 1 Km. The instrument encountered the base approximately 4 Km North-Northeast of the release point at the NASA Glenn Researcher Center (GRC) hangar parking lot, roughly 0.4 Km East of the NIRSS ground instrumentation. Both NIRSS and 20140301-001 indicated the greatest SLWC concentration towards the cloud top at an altitude of 3 Km. The calculated ILW value from 20140301-001 is 0.12 mm, and the radiometer-derived ILW is 0.26 mm.

The 20140301-002 package was released 52 min after 20140301-001, indicating cloud base around 2 Km, approximately 1 Km above the freezing layer. The cloud base was again encountered around 4 Km North-Northeast of the release location; within 1 Km of the location 20140301-001 entered the cloud layer. The second package indicated a marked thinning of the icing layer. Again, both the instrument package and the NIRSS indicate the greatest concentration of SLWC towards the cloud top. The ILW from the 201403001-002 sounding profile is 0.04 mm, and 0.09 mm from the NIRSS.

The NIRSS temperature and dew point profiles are included in the Skew-T, Log-P diagrams for purposes of comparison. The indicated freezing layer from the instrument packages and NIRSS agree to within a 0.1 Km for both releases on March 01.

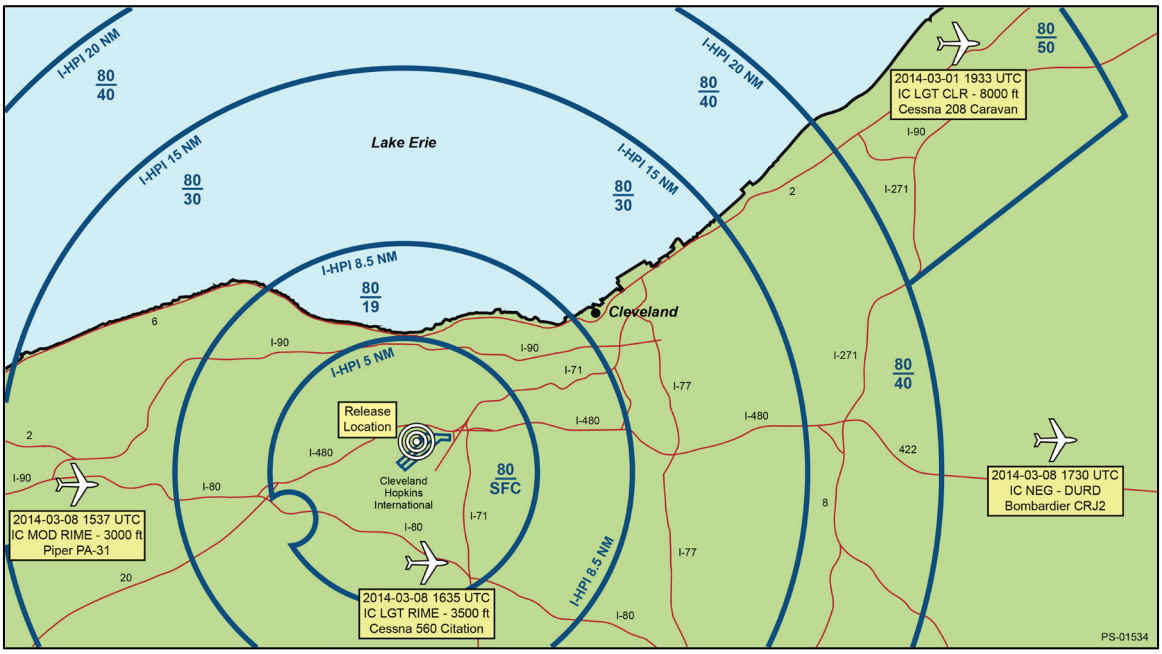

Figure 14.—Cleveland Hopkins International Airport Sectional Chart showing instrument package release location and relevant icing PIREP location and information from March 01, 2014 and March 08, 2014.

Figure 14 is a simplified sectional aeronautical chart for the Cleveland Hopkins International Airport with the locations and information for several Pilot Reports (PIREP) identifying icing conditions from March 01 and March 08. A single PIREP, from a Cessna 208 Caravan, was reported March 01, 41 min prior to the first release. Light clear icing was observed at a flight level of approximately 2.4 Km, 45 Km Northeast of the release location. The maximum calculated SLWC from 20140301-001 was at a pressure altitude of approximately 2.8 Km.

4.2 March 8, 2014 Soundings

Three instrument packages were released on March 08, 2014 from the NASA GRC hangar parking lot; the first (20140308-001) at 14:38 UTC, the second (20140308-002) at 16:52 UTC and the third (20140308-003) at 17:43 UTC. The final data for all three releases is shown in Figures 15 to 17, and relevant PIREPs from March 08 are included in Figure 14.

The measured temperature was at or below freezing for all three soundings, and very light snow precipitation was observed starting just prior to the second balloon release. Reference 14 indicates that ground based microwave radiometer measurements are accurate if the instrument has means to mitigate accumulation of precipitation on the radome. The NIRSS radiometer includes such a system.

The calculated ILW for the 20140308-001 release was 0.11 mm, where radiometer derived-ILW value was 0.35 mm, and the 20140308-002 ILW values are 0.14 mm for the weather balloon, and 0.43 mm for the radiometer. There is less agreement between the weather balloon SLWC and the NIRSS profiles for both the 20140308-001 and 20140308-002 soundings, as seen in Figures 15 and 16, than the soundings from March 01.

A Piper PA-31, 27 Km West of the release location, reported moderate rime at 0.9 Km, 59 min after the first March 08 sounding. Additionally, a Cessna 560 Citation, approximately 10 Km South of the release location, reported light rime at a flight level just above 1 Km, 17 min prior to the second sounding. The profile in Figure 15 from the first sounding indicates a layer of SLWC peaking at approximately 0.7 Km, and Figure 16 from the second sounding indicates a localized layer peaking just above 1 Km.

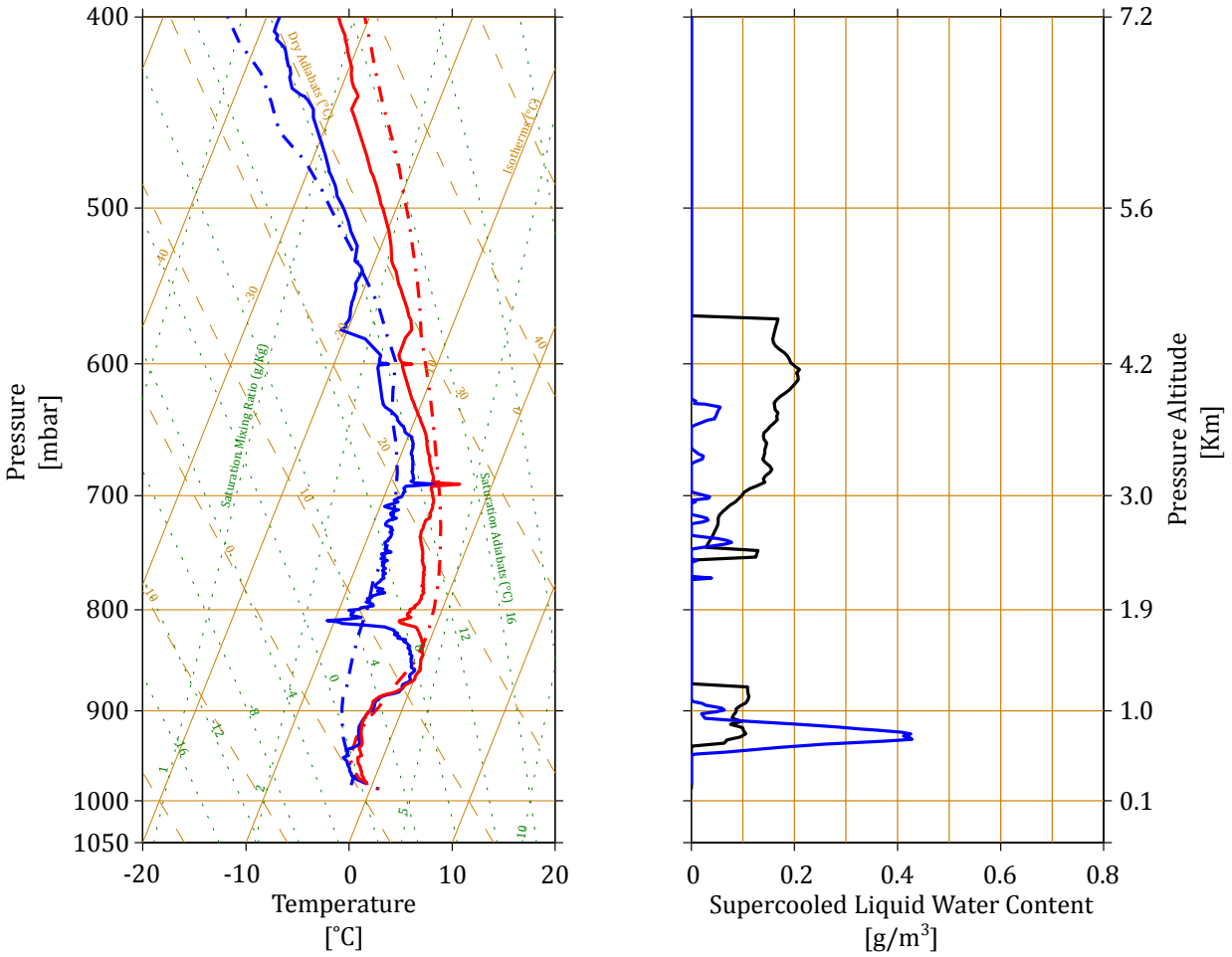

Figure 15.—March 08, 2014 Release 01 Final Data; (left) Skew-T, Log-P Diagram showing temperature (red) and dew point (blue) for the instrument package (solid) and NIRSS (dashed), and (right) the corresponding, calculated SLWC from Equation (26) (blue) and NIRSS (black).

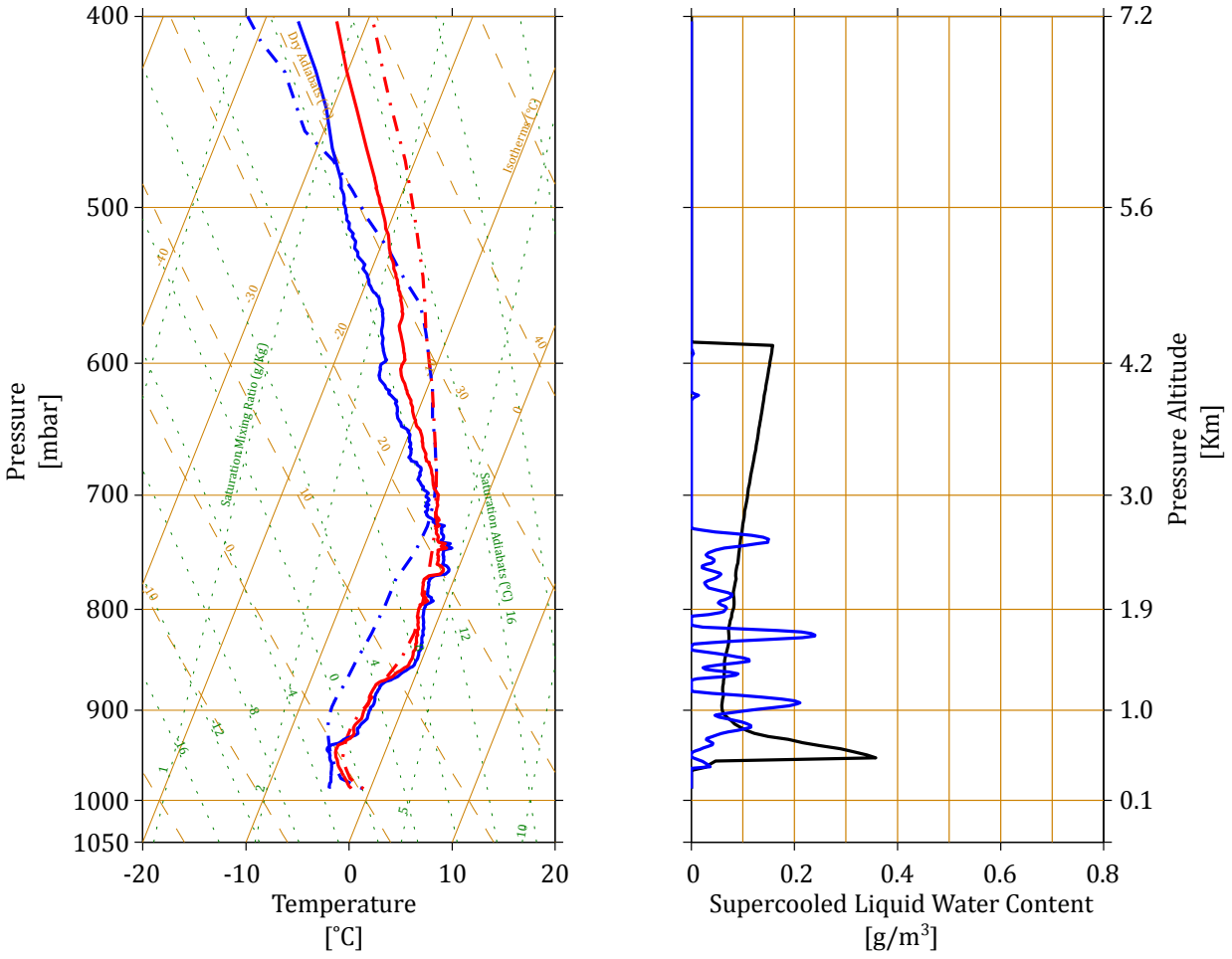

Figure 16.—March 08, 2014 Release 02 Final Data; (left) Skew-T, Log-P Diagram showing temperature (red) and dew point (blue) for the instrument package (solid) and NIRSS (dashed), and (right) the corresponding, calculated SLWC from Equation (26) (blue) and NIRSS (black).

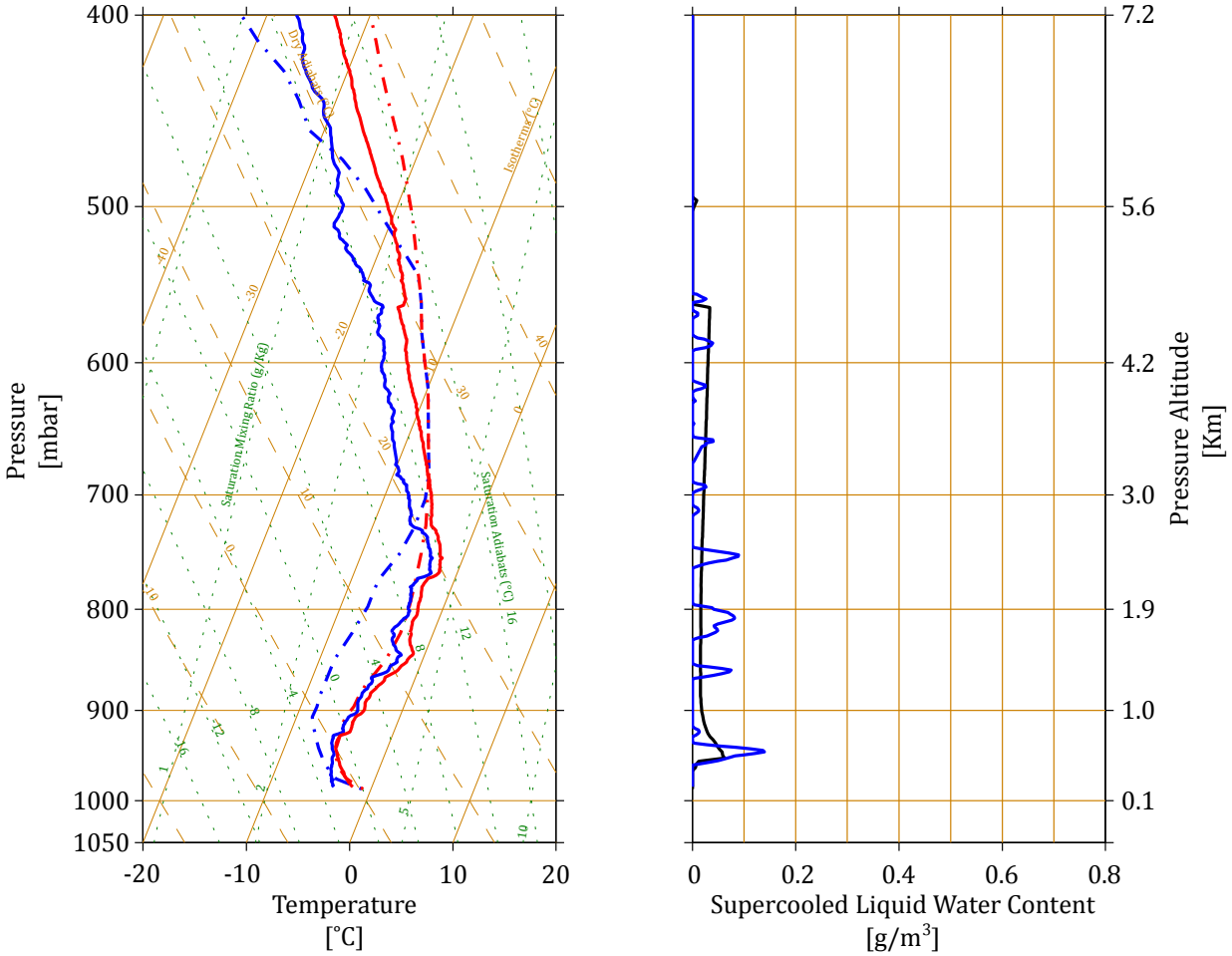

Figure 17.—March 08, 2014 Release 03 Final Data; (left) Skew-T, Log-P Diagram showing temperature (red) and dew point (blue) for the instrument package (solid) and NIRSS (dashed), and (right) the corresponding, calculated SLWC from Equation (26) (blue) and NIRSS (black).

The 20140308-003 sounding, shown in Figure 17, represents a good null case. Both the in-situ and the NIRSS profiles indicate negligible SLWC aloft. A Bombardier CRJ2 reported negative icing during decent 13 min prior to this release, approximately 44 Km East of the release location.

5.0 Discussion

An analysis method to handle the outliers in the telemetry and smooth the frequency data was developed and presented to support NIRSS validation efforts. Additionally, a mathematical model was developed to analyze the data obtained during March 2014 using weather balloons. The limitations of the model developed during this research and the model derived by the original developer were outlined. It was shown that the effect of ice stiffness might not be negligible when the sensor is exposed to conditions that lead to significant ice accretion along the wire.

The analysis method and model were applied to the in-situ measurements obtained during March 01, 2014 and March 08, 2014, and the results were compared to the NIRSS and PIREPs. Previous works (Refs. 5, 12, and 13) have indicated good agreement (±15 percent) of radiometer-derived ILW with in-situ measurements from aircraft. The reasons for the increased disagreement between the ILW values obtained from the in-situ and ground instrumentation used in this study remain unclear. The sources of disagreement may include the spatial and temporal resolution differences between the in-situ and ground

measurements. These differences are outlined further in Reference 5. Deficiencies in the model, including the assumed ice accretion cross-section and distribution, the collection efficiency and the assumed MVD are also likely contributing factors. However, the SLWC profiles between the ground and airborne instrumentation from March 01, 2014 appear to have acceptable agreement. There is disagreement between the two systems for the first two soundings from March 08, 2014. However, the PIREPs from March 08 indicate qualitative agreement with the SLWC sensors. The third sounding represents a null case where the ground and airborne instrumentation agree. Additionally, a scaling issue in the NIRSS code when calculating the SLWC profile was discovered as a result of this research, and a method to address this issue was outlined and applied.

Additional investigation is necessary to further define the behavior of vibrating wire SLWC sensors, including a thorough calibration effort. Anasphere, Inc. has conducted such an effort in 2015 as a part of a NASA sponsored effort. Further work could include examination into the effect of mixed and glaze ice shapes to quantify the theoretical response of the vibrating wire to such accretions. Additionally, in-situ comparisons to instrumented aircraft are desired to address potential spatial variations and provide cloud drop size reference data. The results of this work are the first steps in the effort to validate the NIRSS, which could lead to improved flight safety for the aviation community through remote detection of inflight icing conditions.

References

1. Reehorst, A., Serke, D., "A Terminal Area Icing Remote Sensing System," NASA/TM—2014-218417, Nov 2014.
2. Hill, G.E. and Woffinden, D., "A Balloonborne Instrument for the Measurement of Vertical Profiles of Supercooled Liquid Water Concentration," Journal of Applied Meteorology, Volume 19, 1285–1292, 1980.
3. Hill, G.E., "Laboratory Calibration of a Vibrating Wire Device for Measuring Concentrations of Supercooled Liquid Water," Journal Atmospheric and Oceanic Technology, Volume 6, 961–970, 1989.
4. Hill, G.E., "Analysis of Supercooled Liquid Water Measurements Using Microwave Radiometer and Vibrating Wire Devices," Journal of Atmospheric and Oceanic Technology, Volume 11, 1242–1252, 1994.
5. Serke, D., et al., "Supercooled Liquid Water Content Profiling Case Studies With a New Vibrating Wire Sonde Compared to a Ground-based Microwave Radiometer," Atmospheric Research, Volume 149, 77–87, 2014.
6. Hibbeler, R.C., "Statics and Mechanics of Materials," 2nd Ed. Pearson Prentice Hall, Upper Saddle River, N.J., 2004, Chapter 6, 1980.
7. Mellor, M., "Mechanical Behavior of Sea Ice," CRREL Monogr., No. 83-1, U.S. Army Cold Regions Research and Engineering Laboratory, 1983.
8. Vargas, M., et al., "Local and Total Density Measurements in Ice Shapes," NASA/TM—2005-213440, Mar 2005.
9. Brun, R.J., W. Lewis, P.J. Perkins, and J.S. Serafini, "Impingement of Cloud Droplets on a Cylinder and Procedure for Measuring Liquid-Water Content and Droplet Sizes in Supercooled Clouds by Rotating Multicylinder Method," NASA Report No. 1215, Washington DC, 1954.
10. Langmuir, I., and Blodgett, K., "A Mathematical Investigation of Water Droplet Trajectories. Army Air Forces Tech. Rep. No. 5418, 1946.
11. Lozowski, E.P., Stallabrass, J.R., Hearty, P.F., "The Icing of an Unheated, Nonrotating Cylinder Part I: A Simulation Model," Journal of Climate and Applied Meteorology. Volume 22, 2053–2062, 1983.
12. Westwater, E., "The Accuracy of Water Vapor and Cloud Liquid Determination by Dual-Frequencry Gound-based Microwave Radiometer," Radio Science, 13, 677–685, July-August 1978.

13. Westwater, E., et al., “Analysis of Integrated Cloud Liquid and Precipitable Water Vapor Retrievals from Microwave Radiometers During the Surface Heat Budget of the Arctic Ocean project,” Geophysical Research, 106, 32,019–32,030, December 2001.
14. Ware, R., et al. “Ground-Based Microwave Radiometer Measurements During Precipitation,” Presented at the 8th Specialist Meeting on Microwave Radiometry, 24–27 Feb 2004.
15. Richter-Menge, J., “Static Determination of Young’s Modulus in Sea Ice,” Cold Regions Science and Technology, Volume 9, Issue 3, 283–286, 1984.
16. “The Use of the Skew T, Log P Diagram in Analysis and Forecasting,” AWS/TR-79/006 (Revised), 1990.